Mechanical Systems and Signal Processing 136 (2020) 106485

Contents lists available at ScienceDirect

Mechanical Systems and Signal Processing

journal homepage: www.elsevier.com/locate/ymssp

Detection and isolation of Tollmien-Schlichting waves in shear flows using blind source separation

Igal Gluzman *, Yaakov Oshman, Jacob Cohen

Faculty of Aerospace Engineering, Technion – Israel Institute of Technology, Haifa 32000, Israel

ARTICLE INFO

Article history:
Received 18 November 2018
Received in revised form 18 October 2019
Accepted 27 October 2019
Available online 15 November 2019

Keywords:
Blind source separation
Independent component analysis
Tollmien-Schlichting waves
Flow measurements
Transitional boundary layer

ABSTRACT

A blind source separation (BSS) method for the detection and isolation of Tollmien-Schlichting (TS) waves in sub-critical transitional shear flows is presented. The method is based on an adaptation of the celebrated independent component analysis (ICA) technique to the problem at hand, using appropriate modeling of the flow field and the disturbances acting on it. This modeling is founded on the representation of the acquired flow measurements as mixtures (generated by an a priori unknown mixing process) of disturbance sources. Only the disturbance mixtures, as measured by the sensors embedded in the flow field, are input to the new method. Linear stability theory (LST) is used to model the measured mixtures of sources acquired by sensors placed in the shear flow field. A physics-based design criterion, assuming prior knowledge of the TS wavelengths, is derived for proper sensor placement in order to successfully separate TS wave disturbances. The criterion is verified both numerically, for wall-bounded shear flows, and experimentally, via a wind-tunnel experimental study of flow over a flat plate. The new disturbance detection and isolation approach is expected to prove useful in various applications, including closed-loop flow control problems.

© 2019 Elsevier Ltd. All rights reserved.

1. Introduction

Flow measurements play an important role in various engineering applications. For example, in the aerospace field the obtained flow data can be used in designing aircraft, gaining insights into physical aspects of the flow, validating numerical models that predict the flow, monitoring aircraft flight, and extracting vital information for flow control applications. In order to extract valuable information from raw signal measurements, further processing is usually required. The most common example of signal measurements processing is the projection of the measured data (from the time domain) onto the frequency domain by Fourier transform, whereby we can reveal the dominant frequencies in the flow, a crucial information required for applications such as mentioned above. Another common procedure to treat the measured data is to represent it in the statistical, rather than in the time/frequency domain, as done, e.g., in the proper orthogonal decomposition (POD) technique [1], also known as principal component analysis (PCA) [2]. In POD, the data is projected onto a set of modes, ordered according to their weighted energy. This is then used to deduce information about coherent structures of complex flows from limited data sets acquired by the sensors. For example, in [3], POD is used to estimate the full velocity field from wall pressure measurements over a backward facing ramp. Another powerful method, named dynamic mode decomposition (DMD), is proposed in [4]. DMD can provide temporal dynamic characteristics together with their associated spatial coherent

* Corresponding author at: Department of Mechanical Engineering, Johns Hopkins University, Baltimore, MD 21218, USA.
E-mail addresses: igluzma1@jhu.edu (I. Gluzman), yaakov.oshman@technion.ac.il (Y. Oshman), aerycyc@gmail.com (J. Cohen).

https://doi.org/10.1016/j.ymssp.2019.106485
0888-3270/© 2019 Elsevier Ltd. All rights reserved.

fluid structures obtained from a time series snapshots of measured fields of flow variables. This yields important insights into the physical fluid system, which can then be utilized to effectively delay, or even prevent, the transition from a laminar to a turbulent state.

Physical disturbances, such as those generated by sound or free-stream vorticity, or by artificially generated acoustic, mechanical or electrical actuators, can modify the state of the flow field, by changing the properties of the flow (e.g., fluid velocity, temperature, or pressure) for a given combination of location and time. In this work we regard the flow field measurements, as measured by sensors embedded in the flow field, to consist of mixtures of disturbance sources, where a disturbance source is defined to be the signal recorded by the sensor due to the sole action of a particular physical disturbance. The uniquely identified disturbance sources might provide vital information for designing closed-loop control strategies for flow control applications.

Our approach of identifying the sources from measured mixtures in shear flow is based on adapting blind source separation (BSS) techniques. Known to be very powerful in image processing and acoustical applications, these methods were originally developed to solve the problem of separating linear convolutive mixtures in acoustic applications, known as the *cocktail-party problem*. In that problem, the goal is to identify the sources of speech pressure waves, generated by simultaneously active and independent speakers in the same room [5,6]. Similar applications can be found in brain imaging data for recovering the original components of brain activity from mixed recorded data acquired by an electroencephalogram (EEG). Source separation has also been applied to analyzing astronomical data or satellite images, finding hidden factors in financial data, and reducing noise in natural images. For more applications the interested reader is referred to [6,7] and references therein. Recent developments in BSS methods are based on sparsity-inducing methods, such as the sparse component extraction algorithm that was proposed by [8] for diagnostic imaging system; unsupervised data decomposition techniques, such as the nonnegative matrix factorization (NMF) methodology [9], and their extensions to 3D nonnegative tensor factorization (NTF) [10]. A broad survey of models and efficient algorithms of NMF and NTF for BSS is provided in [11].

We adopt and use the celebrated independent component analysis (ICA) technique as a BSS method in our study. The ICA technique has been extensively developed and used over the past three decades. Although originally developed to deal with problems that are closely related to the *cocktail party problem*, it has also been used in many other applications in the fields of, e.g., signal processing, image processing, artificial neural networks, statistics, and information theory [12,13]. In particular, BSS methods, including ICA, proved useful in mechanical systems applications [14]. Thus, in the field of structural health monitoring, ICA method was used by [15] to detect impact damage in carbon fiber reinforced plastic samples. In that study, ICA was applied for the detection and separation of the influences of different layers, defects, and their combination information from thermal images that were acquired via eddy current pulsed thermography. ICA has also shown rich potential in vibration analysis for condition monitoring and fault diagnosis. For example, [16] used ICA for the detection of signal transients in vibration signals generated by a gearbox. In [17], a fault recognition method was proposed for the speed-up and speed-down processes of rotating machinery, in which ICA was successfully used for redundancy reduction and feature extraction from multi-channel experimental vibration data. ICA has also been applied in modal analysis, e.g., [18], where time-domain structural system identification technique was developed, and the relation between the vibration modes of the mechanical system and the mixing matrix, computed through ICA, was established.

Our research is focused on separating linearly superimposed Tollmien-Schlichting (TS) waves in a boundary layer. Each of these waves is an infinitesimal monochromatic (single frequency) wavy disturbance. Introducing such disturbances to the boundary layer can modify the flow state from laminar to turbulent through certain transition scenarios depending on the disturbance characteristics. Accordingly, the early stages of the transition process are governed by linear mechanisms. Under these conditions, linear stability theory (LST) can predict the downstream evolution of the combined disturbances. To adapt the BSS approach to the problem of disturbance identification in shear flows, we develop a mathematical model expressing the measured mixtures in N_x sensors due to N_s 3D TS disturbances. We assume that the disturbances are infinitesimal, so that they can be described by LST for the spatial case, where they may amplify/decay along the streamwise direction. We study, both numerically and analytically, various sensor-actuator arrangements, and determine sensor placement design conditions that render the ICA BSS method applicable to our problem.

The remainder of this paper is organized as follows. ICA-based BSS methods are briefly summarized in Section 2. The LST-based formulation of source-mixture measurements is given in Section 3. In Section 4 we derive sensor placement design conditions for successful separation of 3D TS disturbances by the ICA method. These conditions are validated numerically and experimentally in Sections 5 and 6, respectively. A summary of our findings and concluding remarks are finally offered in Section 7.

2. The independent component analysis method

The BSS method used in the present work is based on the ICA model of [19],

$$\mathbf{x} = \mathbf{A}\mathbf{s}. \tag{1}$$

Here, $\mathbf{A}$ is an $N_x \times N_s$ matrix containing the mixing coefficients. N_s (assumed independent) sources are denoted by $\mathbf{s} = [s_1\, s_2\, \ldots\, s_{N_s}]^T$, the mixed sources are sensed by an array of N_x sensors, and the acquired signals are denoted by $\mathbf{x} = [x_1\, x_2\, \ldots\, x_{N_x}]^T$. Many algorithms have been developed to address this model, which is also known as the instantaneous

or delayless (linear) mixture model. Many of these algorithms consist of ICA methods that are based on high-order statistics [19]. Therefore, the mixing model in Eq. (1) is also referred to as the linear ICA model. The BSS problem is to estimate, based on the observable random vector $\mathbf{x}$ only, both the mixing matrix $\mathbf{A}$ and the latent variables $\mathbf{s}$. Having estimated the matrix $\mathbf{A}$, one can compute its inverse, $\mathbf{W}$, and obtain the independent components $\mathbf{s}$ as

$$\mathbf{s} = \mathbf{W}\mathbf{x}. \tag{2}$$

ICA is a general name for a variety of techniques that seek to uncover the independent source signals from a set of observations that are composed of linear mixtures of the underlying sources. The method is based on representation of data in the statistical domain. In ICA, the data is projected on a set of axes that imply independence based on statistical criteria of non-Gaussianity. This independence is defined by some measure that is maximized in order to decorrelate the data and determine the axes. Then the sources are projected onto the determined axes. The ICA method offers alternative representation of data in the statistical domain rather than in the frequency domain, as obtained by the Fourier Transform method, in which the data is projected on a set of fixed axes representing discrete frequencies or wavenumbers. By assuming that the sources are independent and non-Gaussian, we can use the central limit theorem (CLT) in order to discover the axes. The CLT states that the distribution of a sum of independent random variables tends toward a Gaussian distribution under certain conditions [20]. Thus, a sum of two independent random variables usually has a distribution that is 'closer' to Gaussian, in some sense, than any of the two original random variables. The idea is to decompose the observed signal into a set of mixtures with distributions that are as non-Gaussian as possible, in order to determine the independent source signals from the measured mixture.

The ICA algorithm is based on a cost-function that consists of a measure of non-Gaussianity. A common criterion of non-Gaussianity can be obtained by using an entropy-based cost function such as negentropy, defined as

$$J(x) \triangleq H(x_G) - H(x_i), \tag{3}$$

Here, x_G is a Gaussian random variable having the same covariance matrix as x_i, and $H(x_i)$ is the entropy, defined through the probability mass function P_{x_i} of the discrete random variable x_i, as

$$H(x_i) \triangleq -\sum_m P_{x_i}(x_i = a_m) \log P_{x_i}(x_i = a_m). \tag{4}$$

A fundamental result of information theory is that a standard Gaussian variable has the largest entropy among all random variables of equal variance [21]. Hence, the negentropy is always non-negative, and it is zero if and only if x_i is Gaussian distributed. The problem in using negentropy, however, is that it is difficult to compute. Therefore, simpler approximations, based on the maximum-entropy principle, are commonly used, e.g.,

$$J(x_i) \propto [\mathbb{E}(g(x_i)) - \mathbb{E}(g(x_{SG}))]^2, \tag{5}$$

where $\mathbb{E}(\cdot)$ denotes the mathematical expectation operator, $x_{SG} \sim N(0,1)$, g is a function defined as either $g(x) \triangleq \frac{1}{c}\log\cosh(cx)$ with $1 \leqslant c \leqslant 2$, or $g(x) \triangleq -e^{-x^2/2}$ in order to obtain more robust estimators [22]. A practical algorithm based on this cost function is the FastICA algorithm. It is based on a fixed-point iteration scheme for finding the maximum non-Gaussianity of $\mathbf{w}^T\mathbf{x}$ by the approximation of negentropy $J(\mathbf{w}^T\mathbf{x})$ in Eq. (5). Here, $\mathbf{w}$ is a weighting vector that is updated by a learning rule that finds the direction $\mathbf{w}$ such that the projection $\mathbf{w}^T\mathbf{x}$ maximizes non-Gaussianity. For details of the algorithm, the reader is referred to [23].

The model in Eq. (1) is based on the following assumptions [12]:

1. Each mixture $x_i(t)$, as well as each component $s_j(t)$, is a random process. For notation simplicity, we omit the time index in the sequel.
2. The components s_i and s_j are statistically independent for all $i \neq j$.
3. The independent components must have non-Gaussian distributions. However, in the basic model, we do not require these distributions to be known (note that if they are known, the problem is considerably simplified).
4. The number of sources is equal to the number of sensors, i.e., $N_s = N_x$. This is a restrictive assumption that can, under certain circumstances, be relaxed [19].
5. Without loss of generality, we assume that both the mixture variables and the independent components have a zero mean, i.e., $E[x_i] = E[s_j] = 0$.
6. For simplicity, noise terms are omitted. It is thus assumed that, when present, the measurement noise is accounted for (i.e., it is reduced or eliminated) prior to implementing the ICA method [12].

In the ICA model of Eq. (1), the following ambiguities hold:

1. Amplitude ambiguity: the variances (energies) of the independent components cannot be determined. The reason is that both $\mathbf{s}$ and $\mathbf{A}$ being unknown, any scalar multiplier in one of the sources s_j can always be canceled by dividing the corresponding column of $\mathbf{A}$ by the same scalar.
2. Sign ambiguity: any independent component can be reversed in sign without affecting the model.
3. Order ambiguity: the order of the independent components cannot be determined because both $\mathbf{s}$ and $\mathbf{A}$ are unknown.

3. Sensor measurement model

To model mixtures of N_s TS wave disturbances that are measured by N_x sensors, we utilize the LST framework under the assumption of parallel flow. When studying the asymptotic stability of the base flow, the equations describing the evolving disturbance can be derived by considering the total flow field as superposition of base $(\mathbf{U}, P)$ and perturbed $(\mathbf{u}^{(1)}, p^{(1)})$ states. The base and the total states satisfy the Navier–Stokes equations. All quantities are nondimensionalized by U_r as a reference velocity (e.g., the free stream velocity) and L_r as a relevant length scale (e.g., the boundary layer thickness at a given streamwise position), yielding the Reynolds number $R = U_r L_r / \nu$ as the governing parameter, where ν is the kinematic viscosity of the flow. Let $\mathbf{U} = [U(y)\, 0\, 0]^T$ be the parallel base flow, i.e., having a velocity component in the x direction that only depends on the wall-normal direction y. By subtracting the equations for the base state from those corresponding to the total state, and dropping the nonlinear terms, the linearized Navier–Stokes (LNS) equations are obtained.

We analyze the stability of the mean flow with respect to wavelike velocity and pressure perturbations, also known as normal modes, for which,

$$q^{(1)} = \hat{q}(y) \cdot e^{i(\alpha x + \beta z - \omega t)}, \tag{6}$$

where $q^{(1)} = [u^{(1)}\, v^{(1)}\, w^{(1)}\, p^{(1)}]^T$, and $\hat{q}(y) = [\hat{u}(y)\, \hat{v}(y)\, \hat{w}(y)\, \hat{p}(y)]^T$ is the corresponding complex eigenvector. We consider the spatial case in which α is a complex eigenvalue; $\alpha_r \triangleq \Re(\alpha)$ and β are the disturbance streamwise and spanwise wavenumbers, respectively; $\alpha_{im} \triangleq \Im(\alpha)$ is the disturbance streamwise decay/growth rate for positive and negative values, respectively, and ω is the disturbance dimensionless frequency. Substituting Eq. (6) into the LNS (which is equivalent to taking its Fourier transform) results in the following *dispersion relation*:

$$\mathbb{D}(\alpha, \beta, \omega) = 0. \tag{7}$$

This constitutes the eigenvalue problem for the complex eigenvalue α and its corresponding eigenfunction $\hat{q}$ for the given spanwise wavenumber β, the real frequency ω, the Reynolds number Re, and the base-flow velocity profile $U(y)$.

In the case of a single wave disturbance measured at a specific height from the wall y_0, Eq. (6) can be written as

$$q(x, y_0, z, t) = |\hat{q}(y_0)| e^{-\alpha_{im} x} \cos(-\omega t + \phi_t(x, y_0, z)). \tag{8}$$

Here, the phase shift in time ϕ_t at y_0 is determined by the spatial parameters of the disturbance,

$$\phi_t(x, y_0, z) \triangleq \alpha_r x + \beta z + \phi(\hat{q}(y_0)) + \phi_{t_0}, \tag{9}$$

where ϕ_{t_0} is the initial phase and x, z denote the current location coordinates of the disturbance on the X-Z plane with respect to the origin, where it was generated, i.e., $[l_x\, l_z] = [x\, z] - [x_0\, z_0]$. Using Eqs. (8) and (9) the expression for the source s_j is given by

$$s_j(x, y_0, z, t) \triangleq |\hat{q}_j(y_0)| \cos(-\omega_j t + \phi_{t_j}(x, y_0, z)). \tag{10}$$

The source s_j is defined as the signal that would have been measured by the sensor if all the other sources were nil. Each source is generated by a particular physical disturbance generator, which characterizes its signature in the sensor recordings. s_j is defined by its frequency ω_j and the initial phase $\phi_{t_{0_j}}$ it had at its introduction location, $\mathbf{r}_{s_j} = [l_x\, l_z]^T_{s_j}$ on the X-Z plane.

In convective flows, the source s_j propagates along the downstream direction. The distance that the disturbance travels to the sensor is

$$L_{x_i s_j} = ||\mathbf{r}_{x_i} - \mathbf{r}_{s_j}||, \tag{11}$$

where $\mathbf{r}_{x_i} = [l_x\, l_z]^T_{x_i}$ is the location of the sensor x_i on the X-Z plane.

Using Eq. (8), the source s_j measured by sensor x_i can be described by

$$s_{ij} \equiv [s_j]_{x_i} = |\hat{q}_j([l_y]_{x_i})| e^{-\alpha_{im_j}([l_x]_{x_i} - [l_x]_{s_j})} cos(-\omega_j t + \phi_{t_{ij}}), \tag{12}$$

where $\phi_{t_{ij}}$ is the phase of source s_j measured at sensor x_i,

$$\phi_{t_{ij}} = \alpha_{r_j}([l_x]_{x_i} - [l_x]_{s_j}) + \beta_j([l_z]_{x_i} - [l_z]_{s_j}) + \phi_j([l_y]_{x_i}) + \phi_{t_{0j}}. \tag{13}$$

Here, $([l_x]_{x_i} - [l_x]_{s_j})$ is the distance that the disturbance travels downstream from the source s_j to sensor x_i, and $([l_z]_{x_i} - [l_z]_{s_j})$ is the distance that the disturbance travels spanwise from the source s_j generation position to sensor x_i position. Thus, source s_j will be recorded at sensor x_i as s_{ij} due to changes in phase $\phi_{t_{ij}}$. The changes in the phase of source s_j at the recorded location of x_i are due to s_j spatial wavenumbers α_{r_j}, β_j and its eigenvector phase $\phi_j(y)$ at the vertical location $[l_y]_{x_i}$ of sensor x_i. Rearranging Eqs. (12) and (13) in vector formulation yields

$$s_{ij} = \left|\hat{q}_j\left([l_y]_{x_i}\right)\right| e^{-\alpha_{im_j}(\mathbf{r}_{x_i} - \mathbf{r}_{s_j}) \cdot \mathbf{e}_x} \cos(-\omega_j t + \phi_{t_{ij}}) \tag{14}$$

$$\phi_{t_{ij}} = \mathbf{a}_j \cdot (\mathbf{r}_{x_i} - \mathbf{r}_{s_j}) + \phi_j([l_y]_{x_i}) + \phi_{t_{0j}} \tag{15}$$

where $\mathbf{a}_j \triangleq \left[\alpha_{r_j}\ \beta_j\right]^T$, and $\mathbf{e}_x$ is the unit vector $\mathbf{e}_x \triangleq [1\ \ 0]^T$. Finally, the sensor measurement x_i due to N_s sources s_j is

$$x_i = \sum_{j=1}^{N_s} s_{ij}, \quad i = 1, 2, \ldots N_x\,. \tag{16}$$

Eq. (16) represents the general model for N_x sensor measurements of N_s TS wave disturbance sources in the form of Eq. (14).

The measurements include $N_x \times N_s$ combinations of s_{ij} recorded by N_x sensors. Each s_{ij} is related to s_j by the change in phase and amplitude due to the traveling distance between source s_j and sensor x_i and the particular characteristics of the source (its associated wavenumbers and frequency) as well as the height of each sensor $i, i = 1, \ldots N_x$.

4. Adaptation to the ICA mixture model

In this section we first show that a straightforward application of the ICA technique to a general problem involving N_x sensors and N_s sources, modeled by the LST framework outlined in Section 3, is impossible. Understanding the inherent incompatibility between the ICA technique and the LST framework facilitates proposing a workaround, in the form of physics-based sensor placement design rules. Complying with these rules guarantees, as shown in this section and demonstrated in the next sections, successful implementation of the ICA disturbance detection and isolation method.

4.1. The general case: N_s sources, N_x sensors

We first consider the general case, involving N_x sensors and N_s sources. According to the LST model, the acquired sensor measurement is given by Eq. (16). The ICA model requires, on the other hand, that the sources and measurements be related according to

$$x_i = \sum_{j=1}^{N_s} a_{ij} s_j, \quad i = 1, 2, \ldots N_x, \tag{17}$$

where a_{ij} are the terms of the mixing matrix $\mathbf{A}$. The downstream growth or decay of the disturbances is associated with these terms. Comparing Eq. (16) with Eq. (17), we see that, as opposed to the ICA model, that permits only N_s sources $[s_1\, s_2 \ldots s_{N_s}]^T$ linearly mixed and recorded by N_x sensors $[x_1\, x_2 \ldots x_{N_x}]^T$, the LST-based measurement model allows for $N_x \times N_s$ different s_{ij} source terms to be recorded by N_x sensors. This renders the use of ICA methods to identify the sources of the LST model not straightforward. Thus, for ICA to be applied, the number of source terms in the LST model needs to be reduced from $N_x \times N_s$ to N_s. A closer look reveals that the problem stems from the fact that the N_s physical sources are observed as $N_x \times N_s$ sources by N_x sensors. We therefore propose to circumvent this "artificial extra sources" by appropriately positioning the sensors in the flow field. To this end, we next study the sensor positioning conditions under which s_{ij} become proportional to s_j, that is,

$$s_{ij} \propto s_j. \tag{18}$$

First, we relate the source definition, Eq. (10), to the time periodicity of the disturbance having a specific phase, i.e.,

$$s_{ij} \propto \cos(-\omega_j t + \phi_{t_{ij}}). \tag{19}$$

To satisfy Eq. (18) we thus require

$$\phi_{t_{ij}} + 2\pi n_{ij} = \phi_{t_{kj}} + 2\pi n_{kj}$$

where

$$\begin{aligned} &j = 1, \ldots, N_s, \\ &n_{ij}, n_{kj} \in \mathbb{Z}, \\ &i = 1, \ldots, N_x, \quad k = 1, \ldots, N_x, \text{ such that } i < k \end{aligned} \tag{20}$$

In Eq. (20) the term $2\pi n_{kj}$ is the phase shift of the source s_{kj}, i, k are the indices of the sensors (we enforce $i < k$ to avoid duplicates of the same sensor configuration), and j is the index of a specific source.

Next, we observe that, since the ICA method is insensitive to the sign of the signal, it provides some flexibility regarding the placement of the sensors, as, e.g., it cannot distinguish between $\cos(\pi)$ and $\cos(2\pi)$. We exploit this flexibility to minimize the distances between sensors, in order to avoid nonlinear effects caused by the downstream growth of the disturbance. Replacing the terms $2\pi n_{ij}$ and $2\pi n_{kj}$ in Eq. (20) with πn_{ij} and πn_{kj}, respectively, and using Eq. (15), yields

$$\frac{1}{\alpha_{r_j}} \mathbf{a}_j \Delta \mathbf{r}_{x_{ik}} = -(\Delta n_{ikj} + \frac{1}{\pi} \Delta \phi_{ikj}) \frac{\lambda_{TS_j}}{2}$$

where

$$\begin{aligned} &j = 1, \ldots, N_s, \\ &\Delta n_{ikj} \in \mathbb{Z}, \\ &i = 1, \ldots, N_x, \quad k = 1, \ldots, N_x, \text{ such that } i < k \end{aligned} \tag{21}$$

In Eq. (21) $\Delta \mathbf{r}_{x_{ik}} \triangleq (\mathbf{r}_{x_i} - \mathbf{r}_{x_k})$, $\Delta\phi_{ikj} \triangleq \phi_j([l_y]_{x_i}) - \phi_j([l_y]_{x_k})$, $\Delta n_{ikj} \triangleq (n_{ij} - n_{kj})$, and $\lambda_{TS_j} \triangleq \frac{2\pi}{\alpha_{r_j}}$ is TS wavelength. Eq. (21) can be recast as

$$[l_x]_{x_i} - [l_x]_{x_k} = \left\{ \prod_{j=1}^{N_s} [-n_{ikj}\lambda_{TS_j}/2] \right\}^{1/N_s}$$

where

$$\begin{aligned} &n_{ikj} \triangleq \left[\Delta n_{ikj} + \tfrac{\Delta\phi_{ikj}}{\pi} + \tfrac{\beta_j}{\pi}([l_z]_{x_i} - [l_z]_{x_k}) \right], \quad n_{ikj} \in \mathbb{Z} \\ &i = 1, \ldots, N_x, \quad k = 1, \ldots, N_x, \text{ such that } i < k \end{aligned} \tag{22}$$

In Eq. (22), the requirement that n_{ikj} be an integer is equivalent to requiring that the distance between each pair of sensors be an integer number of a TS wavelength, which stems from the need to avoid phase shifts between sensors. The relations between different n_{ikj} are found by considering the downstream distance between sensors i and k ($[l_x]_{x_i} < [l_x]_{x_k}$):

$$[l_x]_{x_i} - [l_x]_{x_k} = ([l_x]_{x_i} - [l_x]_{x_{i+1}}) + ([l_x]_{x_{i+1}} - [l_x]_{x_{i+2}}) + \ldots + ([l_x]_{x_{k-1}} - [l_x]_{x_k}) \tag{23}$$

which yields

$$n_{ikj} = \sum_{m=i}^{k-1} n_{m(m+1)j}$$

where

$$\begin{aligned} &n_{ikj} \in \mathbb{Z}, \\ &j = 1, \ldots, N_s, \\ &i = 1, \ldots, N_x, \quad k = 1, \ldots, N_x, \text{ such that } i < k \end{aligned} \tag{24}$$

Eqs. (22) and (24) provide a criterion for the successful implementation of the ICA method in order to detect and isolate 3D TS wave disturbances in a $N_s \times N_x$ source-sensor system. Based on a priori (physics-based) knowledge of the potential source TS wavelengths, the criterion dictates proper placement of the sensors in the flow so as to maintain compatibility of the ICA algorithm with the LST framework.

4.2. Application to a two-source, two-sensor system

Developed in the previous subsection, the general sensor location criterion is quite complex, and becomes arduous when the number of sensors and sources increases, because of source interdependence. To facilitate an effective numerical and experimental demonstration of the performance of the ICA method, we thus resort to the simplest – yet meaningful – case, entailing two sources measured by two sensors.

In the two-source, two-sensor case, the ICA model of Eq. (17) becomes

$$x_1 = a_{11}s_1 + a_{12}s_2 \tag{25a}$$

$$x_2 = a_{21}s_1 + a_{22}s_2. \tag{25b}$$

According to the LST model, Eq. (16), the acquired signals are

$$x_1 = s_{11} + s_{12} \tag{26a}$$

$$x_2 = s_{21} + s_{22} \tag{26b}$$

where

$$s_{11} \triangleq [s_1]_{x_1} = |\hat{q}_1([l_y]_{x_1})| e^{-\alpha_{im_1}([l_x]_{x_1} - [l_x]_{s_1})} \cos(-\omega_1 t + \phi_{t_{11}}) \tag{27a}$$

$$s_{12} \triangleq [s_2]_{x_1} = |\hat{q}_2([l_y]_{x_1})| e^{-\alpha_{im_2}([l_x]_{x_1} - [l_x]_{s_2})} \cos(-\omega_2 t + \phi_{t_{12}}) \tag{27b}$$

$$s_{21} \triangleq [s_1]_{x_2} = |\hat{q}_1([l_y]_{x_2})| e^{-\alpha_{im_1}([l_x]_{x_2} - [l_x]_{s_1})} \cos(-\omega_1 t + \phi_{t_{21}}) \tag{27c}$$

$$s_{22} \triangleq [s_2]_{x_2} = |\hat{q}_2([l_y]_{x_2})| e^{-\alpha_{im_2}([l_x]_{x_2} - [l_x]_{s_2})} \cos(-\omega_2 t + \phi_{t_{22}}) \tag{27d}$$

with corresponding phases

$$\phi_{t_{11}} = \alpha_{r_1}([l_x]_{x_1} - [l_x]_{s_1}) + \beta_1([l_z]_{x_1} - [l_z]_{s_1}) + \phi_1([l_y]_{x_1}) + \phi_{t_{01}} \tag{28a}$$
$$\phi_{t_{12}} = \alpha_{r_2}([l_x]_{x_1} - [l_x]_{s_2}) + \beta_2([l_z]_{x_1} - [l_z]_{s_2}) + \phi_2([l_y]_{x_1}) + \phi_{t_{02}} \tag{28b}$$
$$\phi_{t_{21}} = \alpha_{r_1}([l_x]_{x_2} - [l_x]_{s_1}) + \beta_1([l_z]_{x_2} - [l_z]_{s_1}) + \phi_1([l_y]_{x_2}) + \phi_{t_{01}} \tag{28c}$$
$$\phi_{t_{22}} = \alpha_{r_2}([l_x]_{x_2} - [l_x]_{s_2}) + \beta_2([l_z]_{x_2} - [l_z]_{s_2}) + \phi_2([l_y]_{x_2}) + \phi_{t_{02}} \tag{28d}$$

A comparison of Eq. (25) with Eq. (26) shows that, whereas the ICA model considers only two sources, s_1 and s_2, linearly mixed and recorded in two sensors, x_1 and x_2, the measurement obtained according to the LST model has four different sources, $s_{11}, s_{12}, s_{21}, s_{22}$, recorded by the two sensors x_1 and x_2. In this case, Eq. (22) reduces to

$$[l_x]_{x_1} - [l_x]_{x_2} = \left\{\frac{n_{121}}{2}\lambda_{TS_1}\frac{n_{122}}{2}\lambda_{TS_2}\right\}^{1/2} = \frac{n_{121}}{2}\lambda_{TS_1}, \tag{29}$$

with

$$\frac{\lambda_{TS_2}}{\lambda_{TS_1}} = \frac{\alpha_{r_1}}{\alpha_{r_2}} = \frac{n_{121}}{n_{122}} \in \mathbb{Q}. \tag{30}$$

In Eq. (29),

$$n_{12j} = \left[\Delta n_{12j} + \frac{\Delta\phi_{12j}}{\pi} + \frac{\beta_j}{\pi}([l_z]_{x_1} - [l_z]_{x_2})\right]. \tag{31}$$

Positioning the sensors so as to satisfy Eq. (29) yields

$$\cos(-\omega_1 t + \phi_{t_{11}}) = \cos(-\omega_1 t + \phi_{t_{21}}) \tag{32a}$$
$$\cos(-\omega_2 t + \phi_{t_{12}}) = \cos(-\omega_2 t + \phi_{t_{22}}) \tag{32b}$$

which motivates the definitions

$$\phi_{t_1} \triangleq \phi_{t_{11}} = \phi_{t_{21}} \tag{33a}$$
$$\phi_{t_2} \triangleq \phi_{t_{12}} = \phi_{t_{22}} \tag{33b}$$

and the LST model is recast in ICA form, $\mathbf{x} = \mathbf{A}\mathbf{s}$, where

$$\mathbf{x} = \begin{bmatrix} x_1 \\ x_2 \end{bmatrix} \tag{34a}$$
$$\mathbf{s} = \begin{bmatrix} \cos(-\omega_1 t + \phi_{t_1}) \\ \cos(-\omega_2 t + \phi_{t_2}) \end{bmatrix} \tag{34b}$$
$$\mathbf{A} = \begin{bmatrix} a_{11} & a_{12} \\ a_{21} & a_{22} \end{bmatrix} \tag{34c}$$

and

$$a_{11} = |\hat{q}_1([l_y]_{x_1})|e^{-\alpha_{im_1}([l_x]_{x_1} - [l_x]_{s_1})} \tag{35a}$$
$$a_{12} = |\hat{q}_2([l_y]_{x_1})|e^{-\alpha_{im_2}([l_x]_{x_1} - [l_x]_{s_2})} \tag{35b}$$
$$a_{21} = |\hat{q}_1([l_y]_{x_2})|e^{-\alpha_{im_1}([l_x]_{x_2} - [l_x]_{s_1})} \tag{35c}$$
$$a_{22} = |\hat{q}_2([l_y]_{x_2})|e^{-\alpha_{im_2}([l_x]_{x_2} - [l_x]_{s_2})} \tag{35d}$$

Here, we relate the temporal periodicity and phase shift in the traveling time of the disturbance to the source s_j of the ICA model. The downstream growth or decay of the disturbance is related to the entries of the mixing matrix of the ICA model. $|\hat{q}_j([l_y]_{x_i})|$ is the amplitude of the eigenfunction q_j that is obtained from the dispersion relation, Eq. (7), at a specific vertical location of the sensor x_i inside the boundary layer. Due to the amplitude ambiguity of the ICA model, this amplitude cannot be determined.

To successfully separate the linear mixture of sources, Eq. (25) should comply with the following conditions, which stem from the ICA underlying assumptions:

1. The sources should be independent, and be present in each mixture.
2. The matrix **A** should be invertible.

The second condition is satisfied if the determinant of the matrix **A** does not vanish, which leads to

$$\left|\hat{q}_1([l_y]_{x_1})\right|\left|\hat{q}_2([l_y]_{x_2})\right|e^{-\alpha_{im_1}([l_x]_{x_1}-[l_x]_{s_1})-\alpha_{im_2}([l_x]_{x_2}-[l_x]_{s_2})} \neq \left|\hat{q}_1([l_y]_{x_2})\right|\left|\hat{q}_2([l_y]_{x_1})\right|e^{-\alpha_{im_2}([l_x]_{x_1}-[l_x]_{s_2})-\alpha_{im_1}([l_x]_{x_2}-[l_x]_{s_1})}. \tag{36}$$

If both sensors are placed at the same height, i.e., $[l_y]_{x_1} = [l_y]_{x_2}$, we obtain the following condition:

$$(\alpha_{im1} - \alpha_{im2})([l_x]_{x_2} - [l_x]_{x_1}) \neq 0. \tag{37}$$

From Eq. (37), one may conclude that the location of the sources ($\mathbf{r}_{s_j}$) does not affect the invertibility of $\mathbf{A}$. Nevertheless, the location of the sources does determine the phase of the sources s_{ij}.

Combining these findings with the condition derived in Eq. (29), we conclude that the ICA method can be used in the case of a two-source, two-sensor system if

$$([l_x]_{x_2} - [l_x]_{x_1}) = \frac{n}{2}\lambda_{TS_1}, \tag{38a}$$

such that

$$\frac{\lambda_{TS_2}}{\lambda_{TS_1}} = \frac{\alpha_{r_1}}{\alpha_{r_2}} = \frac{n_{121}}{n_{122}} \in \mathbb{Q}_{>0}. \tag{38b}$$

Eq. (38) states that $\frac{\alpha_{r_1}}{\alpha_{r_2}}$ should be approximated by a positive rational number $\frac{n_{121}}{n_{122}}$. This approximation is constrained by the condition that the distance traveled by the disturbances, from their initiation locations to the sensors, does not exceed the linear region beyond which nonlinear interactions take place.

In passing, we note that, while the mathematical foundation of the ICA method is rooted in the theory of random processes, it has been demonstrated to work very well with mixtures of deterministic signals [19]. For example, [24] shows that ICA can separate mixtures of deterministic sinusoidal signals. Their theoretical investigation is backed by numerical simulations and experimental data. [25,26] addressed the plausibility of applying the ICA method to deterministic signals in the context of geodetic and geophysical applications. They provided a theoretical proof and showed that the ICA method, based on diagonalization of 4th-order cumulant, can be reliably used for exploring the deterministic part of the observed signals, and should perfectly separate an unknown mixture of trend and sinusoidal signals in the data.

5. Numerical study

In this section we implement the LST model for simulating measured mixtures for the two source, two sensor configuration outlined in Eq. (26). Various sensor-actuator arrangements are considered. We consider the downstream propagation of two small disturbances according to the LST model for Plane Poiseuille Flow (PPF) and Blasius Boundary Layer (BBL), as described schematically in Fig. 1. All terms are normalized by reference velocity and length scales associated with each flow. Results from the application of the ICA method to the simulated measurements in shear flows are validated against our theoretical analysis.

The dispersion relation in Eq. (7) is solved for the spatial case by the following system of equations,

$$\begin{bmatrix} 0 & -D & -i\beta & 0 & 0 & 0 \\ 0 & 0 & 0 & 0 & 1 & 0 \\ 0 & 0 & 0 & 0 & 0 & 1 \\ C & T & iU\beta & 0 & -D/Re & -i\beta/Re \\ 0 & -ReC & 0 & ReD & ReU & 0 \\ 0 & 0 & -ReC & i\beta Re & 0 & ReU \end{bmatrix} \begin{bmatrix} \hat{u} \\ \hat{v} \\ \hat{w} \\ \hat{p} \\ \hat{v}_x \\ \hat{w}_x \end{bmatrix} = i\alpha \begin{bmatrix} \hat{u} \\ \hat{v} \\ \hat{w} \\ \hat{p} \\ \hat{v}_x \\ \hat{w}_x \end{bmatrix}, \tag{39}$$

with homogeneous boundary conditions. For example, in BBL: $\hat{u}, \hat{v}, \hat{w}, \hat{v}_x, \hat{w}_x = 0$ at $y = 0$ and $y \to \infty$ (see Fig. 1). Here C and T denote linear operators, $C \triangleq i\omega + (D^2 - \beta^2)/Re$, and $T \triangleq UD - U_y$. The subscript $(\cdot)_y$ and D represent the first derivative with respect to y, whereas, $(\cdot)_x$ represents the first derivative with respect to x. Thus, we have a boundary value problem (BVP) for

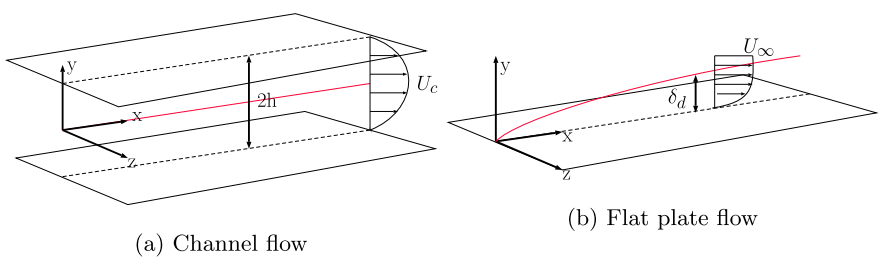

(a) Channel flow (b) Flat plate flow

Fig. 1. Schematic descriptions of PPF and BBL shear flows.

the above system, which we solve numerically with the aid of Matlab utilizing spectral methods ([27]) in which 150 grid points are used. The results of the numerical dispersion-relation solution are validated against reported results in the literature for BBL ([28–30]) and PPF ([31,30]).

Eq. (29) shows that n_{ikj} should be set to be an integer. We can do this by adjusting the proper placement of the sensors in spanwise, streamwise, and vertical locations in the flow to ensure that $\frac{\beta_j}{\pi}([l_z]_{x_i} - [l_z]_{x_k}) \in \mathbb{Z}$ and $\frac{\Delta\phi_{ikj}}{\pi} \in \mathbb{Z}$ in Eq. (22). For simplicity, we consider 2D disturbances (in which $\beta = 0$). This automatically satisfies $\frac{\beta_j}{\pi}([l_z]_{x_i} - [l_z]_{x_k}) \in \mathbb{Z}$.

We consider air as the fluid in both flows (the PPF and the BBL), having a kinematic viscosity of $\nu = 0.15 \times 10^{-4}$ m^2/s. The disturbance sources are introduced in different downstream locations ($\mathbf{r}_{s_j}$) with different frequencies and initial phases. For each flow case, we display two different cases in which we introduce two different sources at different locations. Each source has a certain frequency that dictates its spatial downstream evolution. For specific frequency and downstream injection positions of the source, we have the nondomentional frequency ω and local Reynolds number Re, which are used to solve the dispersion relation and obtain α and q. We set the sensors to measure the streamwise component of the flow, i.e., $q = u$. The obtained eigenvalues α and eigenfunctions u are used in simulating the source mixtures measured by the sensors, as modeled using the LST model. The simulations are performed in dimensional form. Consequently, the dimensionless parameters have to be first rescaled according to the characteristic scales of each flow.

Actual ICA-based source separation is done by the FastICA algorithm of [19]. In particular, we use FastICA Version 2.5 which allows choosing a nonlinear contrast functions $g(x)$ for getting an approximation of negentropy in (5). In our study, the following non-quadratic functions were proven to be very useful: $g(x) \triangleq \frac{1}{c}\log\cosh(cx)$ with $1 \le c \le 2$; $g(x) \triangleq -e^{-x^2/2}$, and also $g(x) \triangleq 0.25x^4$ that correspond to the fourth power as in kurtosis and is justified on statistical grounds for estimating sub-Gaussian independent components, e.g., sinusoidal sources, when there are no outliers. In contrast to many other ICA methods, these estimators work for (practically) any distributions of the independent components and for any choice of the contrast function. The choice of one of the denoted contrast functions $g(x)$ is only important if one wants to optimize the performance of the method. A more detailed discussion regarding the choice of these functions is provided in [23].

We validate the ICA results by comparing them to theoretical predictions that are obtained via LST, assuming known sources and mixing process. Because we focus on sinusoidal signals, we evaluate the method's performance by plotting their time signatures and corresponding Fourier transforms, which facilitates determining if the estimated sources are contaminated by the presence of other sources.

5.1. Application to PPF

The Reynolds number is defined as $Re = U_c h/\nu$, based on the centerline velocity $U_c = 8.5$ m/s and the half-channel height h. In Fig. 2 we display the obtained α_j corresponding to s_j, for each of the two representative cases, Case (a) and Case (b), fulfilling the conditions for successful ICA application. In Case (a) we set $Re = 11,000$ ($h = 19.4$ mm) and consider two sources growing downstream, whereas in the Case (b) we set $Re = 6000$ ($h = 10.6$ mm), and consider two decaying sources.

In Fig. 3, we plot the corresponding eigenfunctions for the streamwise component of velocity ($u = |u|e^{\phi_u}$). From the plotted phase distributions in Fig. 3, we see that the condition of $\frac{\Delta\phi_{ikj}}{\pi} \in \mathbb{Z}$ is satisfied. The phase shift occurs at a specific point (the centerline of the channel) with jumps of integer numbers of π. In the two cases, both sensors are placed at the same vertical position.

We set the downstream distance between the sensors according to Eq. (38). The corresponding results are shown in Fig. 4. In both Case (a) and Case (b), the ratio $\frac{\alpha_{r_1}}{\alpha_{r_2}}$ is approximated to the nearest rational number (up to 3 digits), i.e., $\frac{\alpha_{r_1}}{\alpha_{r_2}} \approx \frac{n_{121}}{n_{122}}$ ($n_{121}, n_{122} < 1000$).

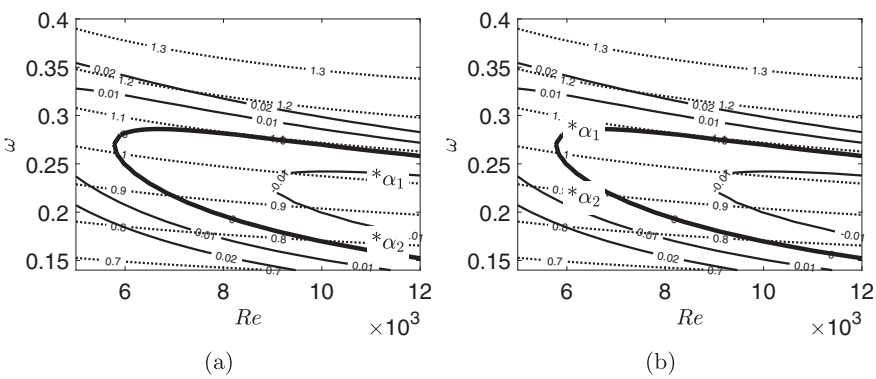

Fig. 2. PPF in Case (a) and Case (b). Sources are introduced at specific (Re, ω), denoted by the asterisk symbols, plotted over contours of constant streamwise wavenumber α_r (dotted black contours), growth rate α_{im} (solid black contours). The neutral curve is denoted by the thick black contour.

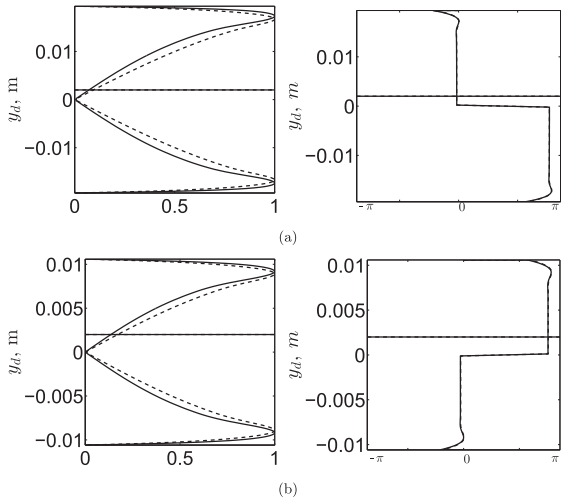

Fig. 3. Streamwise component u: eigenfunction amplitude normalized by its maximum (left), eigenfunction phase of sources (right): s_1 (solid line), s_2 (dashed line). The sensors' vertical positions in the flow are denoted by the horizontal black solid line (Sensor 1) and the black dashed line (Sensor 2). PPF in Case (a) and Case (b).

The measurements generated by the LST model with their Fourier transforms are displayed in Fig. 5. In Case (a) we see the coexistence of both sources in each sensor measurement, whereas in Case (b) the appearance of the second frequency in sensor x_2 is weak.

The results of source separation are depicted in Fig. 6. As expected from our analytic analysis, the separation is successful in each case, that is, we can identify both sources with their correct frequencies. The separation is successful even though in Case (b), one of the sources is almost absent in the sensor measurement (mixture). This demonstrates that the ICA technique is robust with respect to small violations of its underlying assumptions.

5.2. Application to BBL

In this section we consider the flow over a flat plate with zero-pressure-gradient (BBL) for two different cases, denoted as Case (a) and Case (b). In describing the disturbance evolution, the quasi-parallel approach (local stability analysis) is utilized.

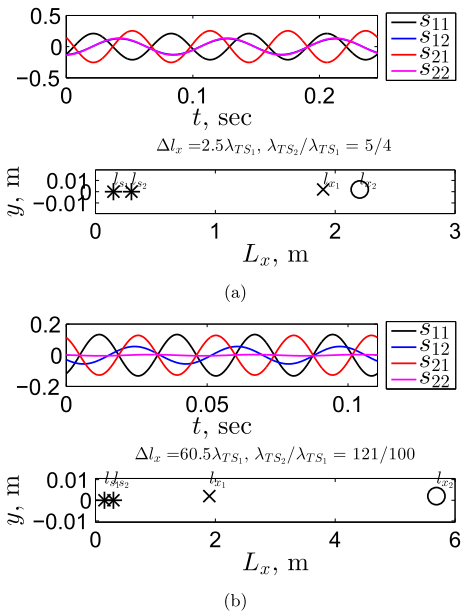

Fig. 4. Signals s_{ij} for two source configurations, Case (a) and Case (b) in PPF. The source configurations are shown underneath the signal plots. "X" symbol: location of Sensor 1, circle symbol: location of sensor 2. Asterisk symbols: source generation locations.

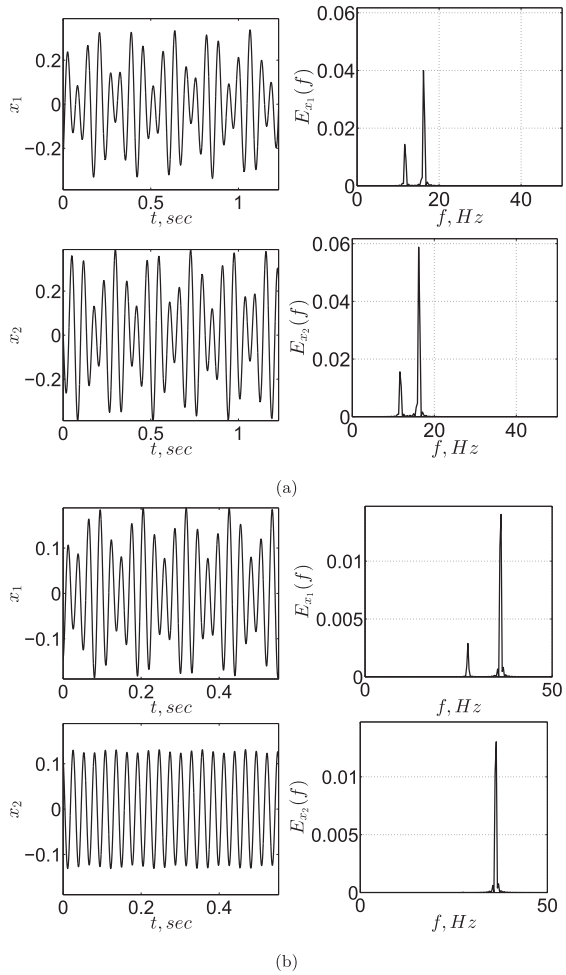

Fig. 5. LST-Simulated measurements of source mixtures (left) and their corresponding Fourier transforms (right). PPF in Case (a) and Case (b).

In BBL we consider the local Reynolds number, $Re(x) = U_\infty \delta_d(x)/\nu$, based on the local displacement thickness δ_d, which for BBL is given by

$$\delta_d(x) = 1.7208\sqrt{\nu x/U_\infty}, \tag{41}$$

and the free-stream velocity U_∞, which is equal to 5 m/s (Case a) and 8.5 m/s (Case b). For each source, we calculate its dimensionless α and u by local stability analysis. These quantities are then rescaled to physical dimensional scales by the local δ_d.

Fig. 7 shows the obtained α_j corresponding to s_j, for two different cases, Case (a) and Case (b). In Case (a) we consider downstream decaying TS modes, and in Case (b) downstream growing TS modes. For each case, both sensors are placed at the same vertical height above the plate.

In Fig. 8, we plot the corresponding eigenfunctions for the streamwise component of velocity ($u = |u|e^{\phi_u}$). The phase profile (ϕ_u) in Fig. 8, shows that the condition $\frac{\Delta\phi_{ikj}}{\pi} \in \mathbb{Z}$ is easily satisfied for a relatively wide range of vertical heights, similarly to the PPF case. The phase profiles have a jump of π around the location of the critical layer where the disturbance phase speed equals the local mean-flow speed.

The variation of phase along the wall-normal distance may be moderate even in the shear layer region, particularly in the cases of 3D disturbances [32]. The chosen vertical locations of the sensors are denoted by the horizontal black line in Fig. 8. For both Case (a) and Case (b), we place the sensors inside the boundary layer near the inner maximum value of $|u|$ profile.

We set the downstream distance between sensors according to Eq. (38), taking into account the downstream growth of the boundary layer. Accordingly, the dimensional ratio between TS wavelengths takes the form of

$$\tilde{k} = \frac{\tilde{\alpha}_{r_1}}{\tilde{\alpha}_{r_2}} = \frac{\alpha_{r_1}}{\alpha_{r_2}} \frac{\delta_{d2}}{\delta_{d1}}. \tag{42}$$

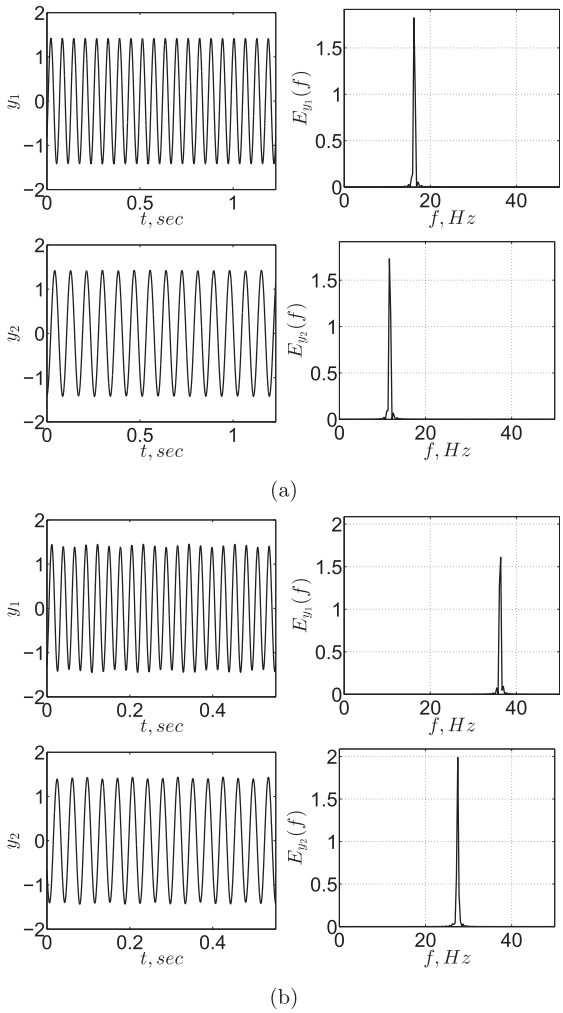

Fig. 6. ICA-estimated sources (left) with their corresponding Fourier transforms (right). PPF in Case (a) and Case (b).

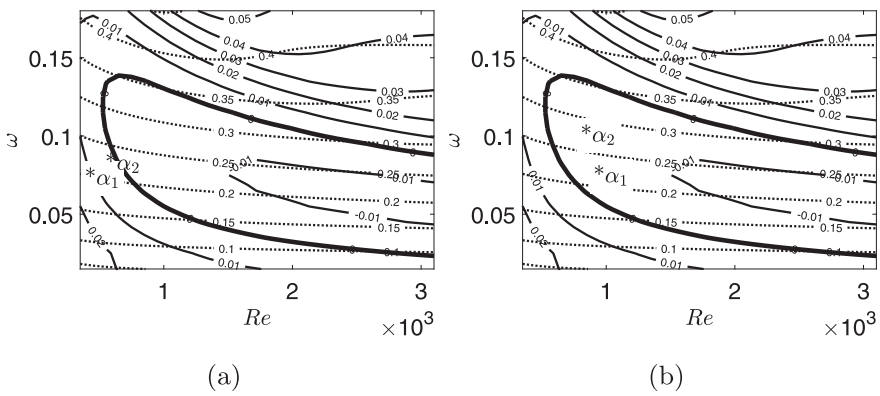

Fig. 7. Introduced sources at specific (Re, ω), denoted by asterisk symbols, plotted over contours of constant streamwise wavenumber α_r (dotted black contours), growth rate α_{im} (solid black contours). The neutral curve is denoted by the thick black contour. BBL in Case (a) and Case (b).

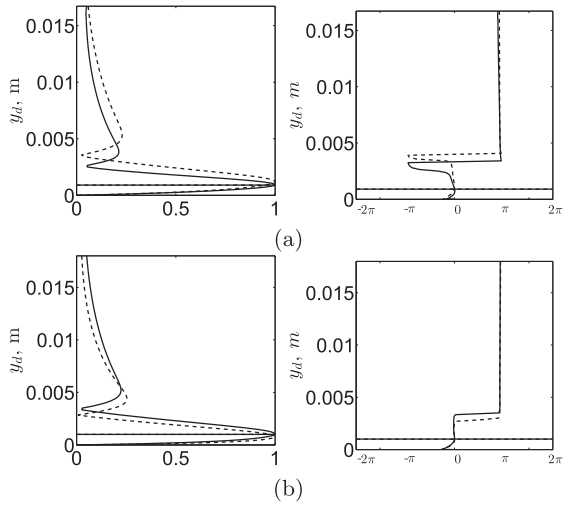

Fig. 8. Streamwise component u: eigenfunction amplitude normalized by its maximum (left), eigenfunction phase of the sources (right): s_1 (solid line), s_2 (dashed line). The sensors' vertical positions in the flow are denoted by the horizontal black solid line (Sensor 1) and the black dashed line (Sensor 2). BBL in Case (a) and Case (b).

The results are shown in Fig. 9. In both Case (a) and Case (b), $\tilde{k}$ is approximated to the nearest rational number (up to single-digit integer number), i.e., $\bar{k} \approx \frac{n_{121}}{n_{122}}$ $(n_{121}, n_{122} < 10)$. In Case (a) we obtain $n_{121}/n_{122} = 6/5$, and for Case (b), we have $n_{121}/n_{122} = 7/10$.

The measurements generated by the LST model with their Fourier transforms are displayed in Fig. 10. The existence of both sources in each sensor measurement is evident. The results of source separation are depicted in Fig. 11. As expected from our analytic analysis, the separation is successful in each case; i.e., both sources are correctly identified with the correct frequencies.

6. Experimental validation

Having validated our method via numerical simulations, in this section we test the method experimentally, using real disturbance mixtures measured in a boundary layer over a flat plate. We focus on BBL flow, which was tested numerically as Case (a) in the previous section.

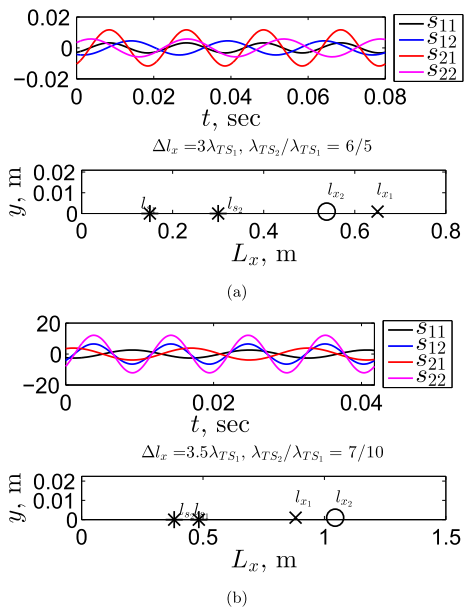

Fig. 9. Signals s_{ij} for two source configurations, Case (a) and Case (b) in BBL. The source configurations are shown underneath the signal plots. "X" symbol: location of Sensor 1, circle symbol: location of Sensor 2. Asterisk symbols: source generation locations.

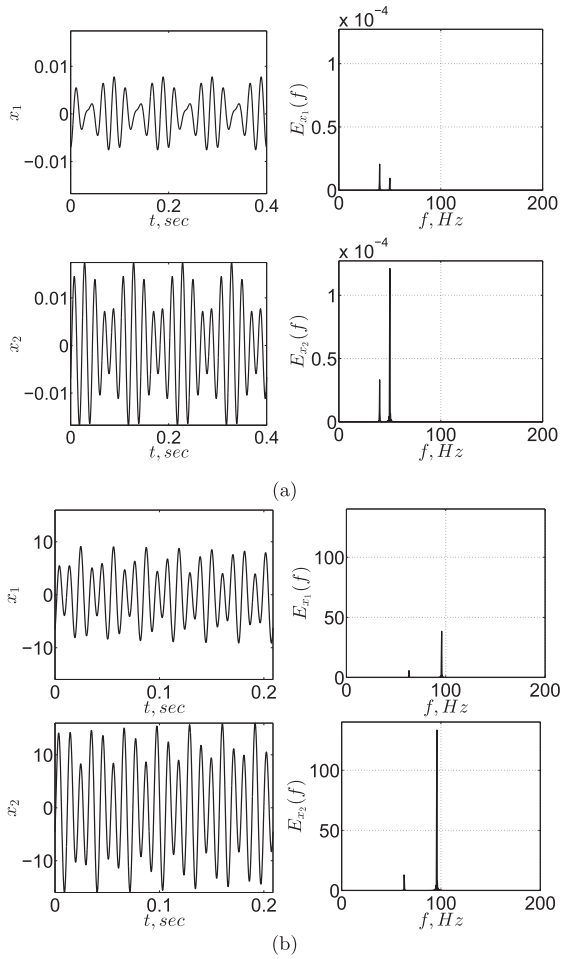

Fig. 10. LST-Simulated measurements of the source mixtures (left) and their corresponding Fourier transforms (right). BBL in Case (a) and Case (b).

The experimental setup is shown in Fig. 12. The plate is made of three combined glass sheets, each 4 mm thick with an asymmetric leading edge according to [33] and a trailing edge flap having an adjustable angle. The leading edge part is designed to minimize the adverse pressure gradient over the region of interest. In addition, by a slight change of the trailing edge flap angle, we can control the stagnation line at the leading edge, thereby preventing boundary layer separation at the leading edge. The plate is 0.45 m wide and 1.4 m long. The trailing edge flap occupies 15% of the total length of the plate. The experiments are performed in a closed-loop wind tunnel with a concentration ratio of 5.76:1, a test section cross area of 0.5 m by 0.5 m, and a length of 1.37 m. The free-stream velocity is set to $U_\infty = 5$ m/s. The turbulence intensity level is 0.15%, measured outside the boundary layer near the leading edge. The streamwise velocity measurements are obtained with the aid of two hot-wires (DANTEC, type 55P11, 5 μm in diameter with a tungsten sensor providing 900 Ω/ft), operated by an A. A. Lab Systems Anemometr. The first sensor (hot-wire 1) is stationary at a fixed location downstream of the leading edge. The second probe (hot-wire 2) is mounted on a traverse system and can be positioned (near Sensor 1) within resolutions of 5 μm in the vertical direction and 1 mm in the streamwise and spanwise directions.

We utilize two single dielectric barrier discharge (SDBD) plasma actuators to artificially generate the disturbance sources [34–36]. Both actuators 1 and 2 are mounted on the plate and placed spanwise parallel to its leading edge and respectively located at $x = 150$ mm and $x = 300$ mm downstream of it. We use copper tape (66 μm thick and 10 mm wide) as the electrodes of each actuator, a glass sheet (4 mm thick) as the dielectric insulation between the electrodes, and the Kapton tape for encapsulation of the grounded electrode. The actuation signal is generated by A-GBS-MiniPuls 2.1 connected to the Cascade RM14 incl Bridge, which is designed for generating high AC voltages with frequencies in the range of 5–20 kHz and amplitudes up to 10 kV peak (=20 kVpp or 7 kVRMS). The device can provide a pulse frequency (burst frequency) in the range of 0–400 Hz and a duty-cycle between 0 and 100% that is suitable for our control applications. The actuators are used for the generation of artificial 2D TS waves by introducing a stationary pulse (with 10% Duty Cycle) signal that, in turn, generates a single frequency disturbance by each actuator. The sources are generated with the minimal possible amplitude, in order to ensure linear interactions. We note, however, that the plasma actuator's input voltage must surpass a certain threshold in

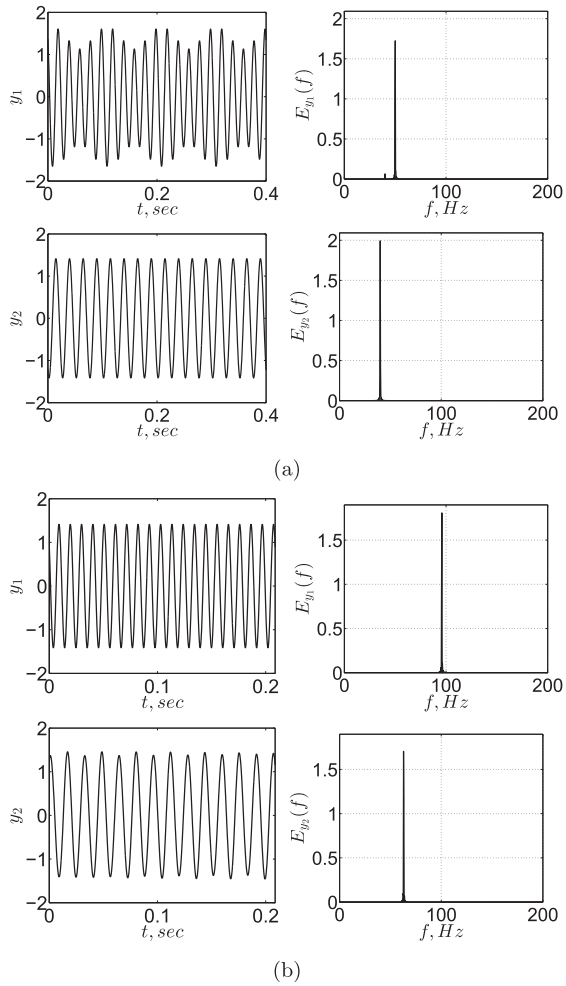

Fig. 11. ICA-Estimated sources (left) with their corresponding Fourier transforms (right). BBL in Case (a) and Case (b).

order to create a uniform discharge along the actuator's span. In addition, appropriate shielding and precautions are used in order to protect the sensor's performance near the actuators.

The two sources introduced to the boundary layer are:

1. s_1: a single frequency disturbance at 50 Hz from actuator 1 (at 150 mm),
2. s_2: a single frequency disturbance at 40 Hz from actuator 2 (at 300 mm).

The selected two frequencies and actuator locations correspond, respectively, to *Re* and ω of the sources of Case (a) in the numerical example for BBL. In the wind-tunnel experiments, each sensor is placed at an approximate height of 1 mm above the plate at the spanwise central region away from plate side edges and test section side walls with a 25 mm spanwise separation (as shown in Fig. 12). The first sensor (Sensor 1) is positioned at 650 mm downstream of the plate leading edge, whereas the second sensor (Sensor 2) is positioned approximately 113 mm upstream of Sensor 1. This distance is selected after considering different locations upstream of Sensor 1 such that $|[l_x]_{x_2} - [l_x]_{x_1}|$ is varied in the range of 108–115 mm with a 1 mm step (the traverse resolution limit). This range is selected according to the numerical results obtained for Case (a) in the BBL numerical example for which Eq. (38) yields $|[l_x]_{x_2} - [l_x]_{x_1}| = 111.8$ mm.

6.1. Signal processing before applying ICA

The measured mixtures of the two sources are contaminated by the free-stream turbulence, background noise, and slow variations of the base flow. Therefore, each measured signal is first preprocessed before applying the ICA method. The following consecutive processing steps are applied to each measured signal:

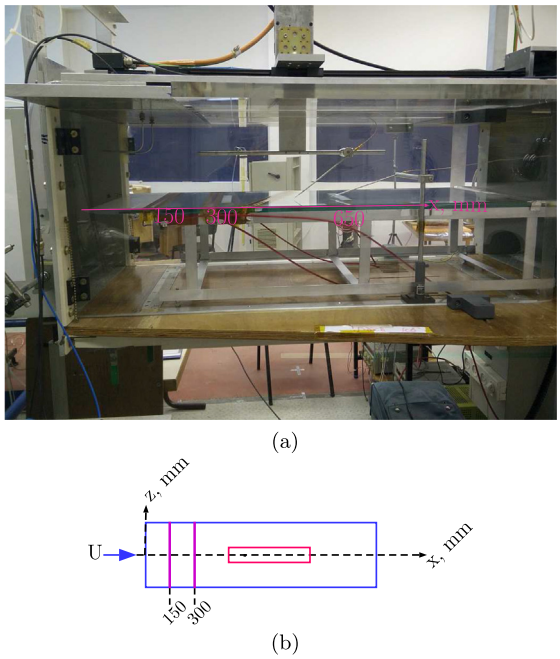

Fig. 12. (a) Experimental setup. (b) Experimental setup scheme: flow over a flat plate equipped with two active plasma actuators. The region of the hot-wire sensor position is denoted by the red rectangle.

1. Prior to recording the signals, hardware low-pass filtering (LPF) is applied so that the filtered signals have a cutoff frequency of 1 kHz. This is done to eliminate the effects of electromagnetic interference (EMI), which is generated by the SDBD plasma actuator. The selected cutoff frequency does not detrimentally affect the measurements because the relevant boundary layer frequencies in this study are below 200 Hz.
2. Next, the signal is detrended, to remove slow variations of the base flow with typical frequencies well below those of the introduced sources. Detrending is performed by subtracting from the signal a smoothed version of it, which is generated by applying a moving average operator to the measured signal. The smoothing window length of the moving average operator is set to smooth out short-term fluctuations of source mixtures, and to highlight longer-term trends of the base flow.
3. The detrended signal is then low-pass filtered, to remove artifacts and noise below 1 kHz, that result from electrical devices, such as the traverse stepper motor noise, and sensor noise, as well as from random flow events or truncation error of the recorded signals. This procedure is done by applying to the recorded signal a moving average operator with a window length designed to ensure that the signal acquisition sample rate is as short as possible but sufficiently long to remove these artifacts.
4. Finally, as required by the ICA method, the signal is centered, by subtracting its computed mean from it.

6.2. Experimental results

The experimental results presented herein correspond to the configuration having Sensor 2 placed 113 mm upstream of Sensor 1. Fig. 13 shows the hot-wire measured mixtures, preprocessed via the procedure outlined in subSection 6.1, along with their corresponding Fourier transforms. As is evident, the signature of each source present in the signal acquired by Sensor 2. In Figs. 13b and 13d the two dominant sources generated by the SDBD plasma actuators appear as single amplitude-peaks at 40 Hz and 50 Hz. In Sensor 1, the first source (50 Hz) is very weak relative to the second source (40 Hz). This can be explained by the decay rates of the disturbances, the disturbance amplitude profiles and the sensor heights with respect to them as shown in Fig. 7a. Furthermore, some additional frequencies are weakly present in the obtained mixtures, such as in the 20 Hz frequency, despite our efforts to create a linear mixture consisting of two TS sources only. The 20 Hz frequency is related to the subharmonic frequency of the second source, thereby indicating the existence of weakly-nonlinear interactions of modulated TS waves in the mixture [37]. Nevertheless, Fig. 14 shows that the ICA technique can still identify and separate the sources. This is attributed to the fact that both sources are comparable in magnitude in the second sensor, and the distance between the sensors satisfies the ICA criterion. One can see that the signature of each estimated source has not been contaminated by the other source.

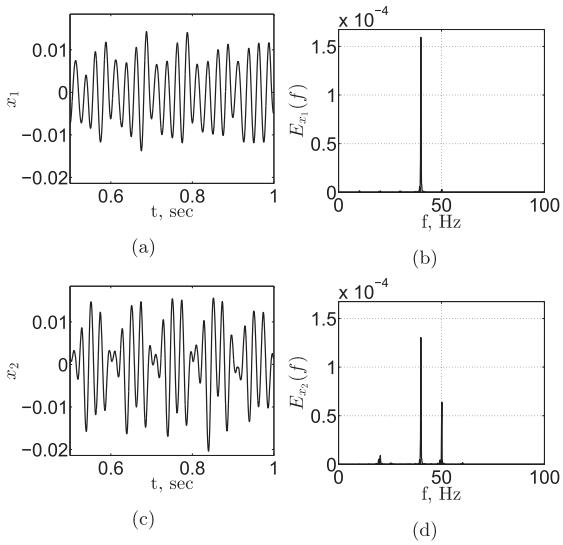

Fig. 13. Measured mixtures in two sensors: (a) x_1, (c) x_2. Mixture Fourier transforms: (b) E_{x_1}, (d) E_{x_2}.

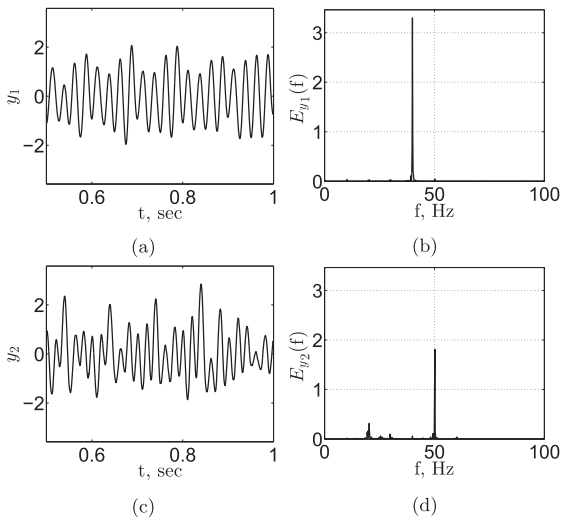

Fig. 14. ICA estimated sources: (a) y_1, (c) y_2. Source Fourier transforms: (b) E_{y_1}, (d) E_{y_2}.

7. Concluding remarks

A BSS-based method has been presented for the detection and isolation of disturbance sources in mixtures measured by sensors in transitional shear flows. LST is invoked to model an N_x-sensors, N_s-sources configuration in shear flow. The LST model is adapted to the ICA form, where the temporal periodicity and phase shift in time of the disturbances are related to the sources of the ICA model. Accordingly, disturbance growth or decay downstream of the flow are related to the entries of the mixing matrix of the ICA model. A physics-based sensor-positioning criterion has been presented, that guarantees successful separation of 3D TS wave disturbances. The criterion requires prior knowledge of the TS source wavelength. The viability of the method is demonstrated via numerical simulations involving PPF and BBL flows. In addition, specially-designed wind tunnel experiments are carried out to demonstrate the performance of the method in a configuration involving two 2D TS disturbances measured by two sensors. Flow over a flat plate is considered, where the sensors are hot-wires, and the source generators are plasma actuators. The experimental results show that the model assumptions can be satisfied by proper placement of sensors in the flow. Moreover, it is shown that the new ICA technique is robust with respect to small imperfections and deviations from its underlying model assumptions.

BSS methods have proved to be very useful in many applications. In this study, the power of ICA has been exploited to enable straightforward extraction of time signatures of TS sources from streamwise velocity measurement signals. In practice, the considered sources are sinusoidal signals, for which Fourier transom can serve as a tool to identify the sources from the observed frequencies in the mixture. However, theoretical background on transitional flows is required to make such a connection. On the other hand, ICA extracts the sources blindly and provides the relation of the frequencies to the corresponding sources directly.

ICA method is based on a different projection support. Unlike the Fourier decomposition, which utilizes the frequency domain, the ICA method is based on the statistical domain. In particular, ICA facilitates decoupled processing and analysis of each source in the time and frequency domains, without affecting or being affected by other sources that comprise the acquired mixture. Therefore, ICA has a potential in fluid mechanics applications for the separation of more complex sources, transient in time, and possessing a rich frequency spectrum in future studies. For example, one may consider the application of ICA on Fourier transformed signals to distinct signal sources at different frequencies in the flow measurements. This approach has been already considered in other disciplines, e.g., [38–40], where the ICA method has been extended and applied on EEG signal mixtures in complex frequency-domain, which allowed to separate sources of rhythmic brain activity better than basic ICA.

In a broader view, ICA offers a new paradigm in which we consider the flow as a mixture of sources, and provide a tool to discover and learn about the mixing process of the flow from the available sensor measurements. In boundary layer studies, the mixing process by itself is very important, and the ability to gain insights into the complex mechanics of the flow-field blindly—from the measured mixtures only—provides a strong motivation to consider BSS methods. Being the most fundamental and extensively studied BSS method, ICA can offer information beyond the source signature; it can also shed light on the mixing process itself, as it can also provide the mixing matrix coefficients.

ICA does have its limitations, but the successful demonstration of its power in the present work (having been validated numerically and experimentally) should motivate future studies that will remedy these limitations and will extend the scope of ICA applications even further than the scope of the present work.

Acknowledgements

The authors wish to thank the following individuals: Oleg Kan and Yefim Shulman, research engineers of the Turbulence Lab of the Technion's Faculty of Aerospace Engineering, for their assistance in designing and constructing the experimental setup; the staff of the Wind Tunnel Complex of the Technion's Faculty of Aerospace Engineering, in particular Mark Koifman, Gilad Benski, Oleg Borochovich, Dror Baraki, and Nadav Shefer, for their vital technical support; Dolev Simon, of the Technion's UAV Workshop, for his assistance in manufacturing the leading edge; David Greenblatt, of the Technion's Faculty of Mechanical Engineering, and David Ashpis of NASA, Cleveland, Ohio, for their professional advice regarding plasma actuator construction and operation. The authors thank the anonymous referees for their insightful comments and suggestions.

References

[1] J.L. Lumley, Stochastic Tools in Turbulence, Academic Press, 1970.
[2] C. Chatfield, A.J. Collins, Principal component analysis, in: Introduction to Multivariate Analysis, Springer, 1980, pp. 57–81.
[3] J. Taylor, M. Glauser, Towards practical flow sensing and control via POD and LSE based low-dimensional tools, J. Fluids Eng. 126 (3) (2004) 337–345.
[4] P.J. Schmid, Dynamic mode decomposition of numerical and experimental data, J. Fluid Mech. 656 (2010) 5–28.
[5] E.C. Cherry, Some experiments on the recognition of speech, with one and with two ears, J. Acoust. Soc. Am. 25 (5) (1953) 975–979.
[6] S. Haykin, Z. Chen, The cocktail party problem, Neural Comput. 17 (9) (2005) 1875–1902.
[7] M.S. Pedersen, J. Larsen, U. Kjems, L.C. Parra, A survey of convolutive blind source separation methods, Multichannel Speech Process. Handb. (2007) 1065–1084.
[8] B. Gao, P. Lu, W.L. Woo, G.Y. Tian, Y. Zhu, M. Johnston, Variational bayesian subgroup adaptive sparse component extraction for diagnostic imaging system, IEEE Trans. Ind. Electron. 65 (10) (2018) 8142–8152, https://doi.org/10.1109/TIE.2018.2801809.
[9] A. Ozerov, C. Fevotte, Multichannel nonnegative matrix factorization in convolutive mixtures for audio source separation, IEEE Trans. Audio Speech Language Process. 18 (3) (2010) 550–563, https://doi.org/10.1109/TASL.2009.2031510.
[10] A. Cichocki, R. Zdunek, S.-I. Amari, Hierarchical als algorithms for nonnegative matrix and 3d tensor factorization, Lecture Notes in Computer Science (including subseries Lecture Notes in Artificial Intelligence and Lecture Notes in Bioinformatics) 4666 LNCS (2007) 169–176.
[11] A. Cichocki, R. Zdunek, A. Phan, S.-I. Amari, Nonnegative Matrix and Tensor Factorizations: Applications to Exploratory Multi-Way Data Analysis and Blind Source Separation, John Wiley & Sons (2009), https://doi.org/10.1002/9780470747278.
[12] A. Hyvärinen, J. Karhunen, E. Oja, Independent Component Analysis, vol. 46, John Wiley & Sons, 2004.
[13] A. Hyvärinen, Independent component analysis: recent advances, Philos. Trans. R. Soc. A 371 (1984) (2013) 20110534.
[14] J. Antoni, S. Braun, Special issue on blind source separation: editorial, Mech. Syst. Signal Process. 19 (2005) 1163–1165.
[15] L. Cheng, B. Gao, G.Y. Tian, W.L. Woo, G. Berthiau, Impact damage detection and identification using eddy current pulsed thermography through integration of pca and ica, IEEE Sens. J. 14 (5) (2014) 1655–1663, https://doi.org/10.1109/JSEN.2014.2301168.
[16] Q. He, Z. Feng, F. Kong, Detection of signal transients using independent component analysis and its application in gearbox condition monitoring, Mech. Syst. Signal Process. 21 (5) (2007) 2056–2071, https://doi.org/10.1016/j.ymssp.2006.09.003.
[17] Z. Li, Y. He, F. Chu, J. Han, W. Hao, Fault recognition method for speed-up and speed-down process of rotating machinery based on independent component analysis and factorial hidden markov model, J. Sound Vib. 291 (1) (2006) 60–71, https://doi.org/10.1016/j.jsv.2005.05.020.
[18] G. Kerschen, F. Poncelet, J.-C. Golinval, Physical interpretation of independent component analysis in structural dynamics, Mech. Syst. Signal Process. 21 (4) (2007) 1561–1575.
[19] A. Hyvärinen, E. Oja, Independent component analysis: algorithms and applications, Neural Netw. 13 (4) (2000) 411–430.
[20] H. Trotter, An elementary proof of the central limit theorem, Arch. Math. 10 (1) (1959) 226–234.
[21] A. Papoulis, Probability, Random Variables, and Stochastic Processes, McGraw-Hill, 1991.

[22] A. Hyvrinen, New approximations of differential entropy for independent component analysis and projection pursuit, Neural Information Processing Systems, vol. 10, 1998, pp. 273–279.
[23] A. Hyvarinen, Fast and robust fixed-point algorithms for independent component analysis, Neural Netw. IEEE Trans. 10 (3) (1999) 626–634.
[24] T. Kirimoto, T. Amishima, A. Okamura, Separation of mixtures of complex sinusoidal signals with independent component analysis, IEICE Trans. Commun. E94.B (2011) 215–221, https://doi.org/10.1587/transcom.E94.B.215.
[25] E. Forootan, J. Kusche, Separation of global time-variable gravity signals into maximally independent components, J. Geodesy 86 (7) (2012) 477–497, https://doi.org/10.1007/s00190-011-0532-5.
[26] E. Forootan, J. Kusche, Separation of deterministic signals using independent component analysis (ica), Stud. Geophys. Geod. 57 (1) (2013) 17–26.
[27] L.N. Trefethen, Spectral Methods in MATLAB, vol. 10, Siam, 2000.
[28] R. Jordinson, The flat plate boundary layer. Part 1. Numerical integration of the orr—sommerfeld equation, J. Fluid Mech. 43 (04) (1970) 801–811.
[29] A.V. Boiko, A.V. Dovgal, G.R. Grek, V.V. Kozlov, Physics of Transitional Shear Flows: Instability and Laminar-Turbulent Transition in Incompressible Near-Wall Shear Layers, vol. 98, Springer, 2011.
[30] P.J. Schmid, D.S. Henningson, Stability and Transition in Shear Flows, vol. 142, Springer Science & Business Media, 2001.
[31] R. Leong, Linear spatial stability of the plane poiseuille flow, AIAA J. 12 (11) (1974) 1605–1607.
[32] J. Cohen, K.S. Breuer, J.H. Haritonidis, On the evolution of a wave packet in a laminar boundary layer, J. Fluid Mech. 225 (1991) 575–606.
[33] J.H.M. Fransson, Leading edge design process using a commercial flow solver, Exp. Fluids 37 (6) (2004) 929–932.
[34] T.C. Corke, M.L. Post, D.M. Orlov, Single dielectric barrier discharge plasma enhanced aerodynamics: physics, modeling and applications, Exp. Fluids 46 (1) (2009) 1–26.
[35] E. Moreau, Airflow control by non-thermal plasma actuators, J. Phys. D: Appl. Phys. 40 (3) (2007) 605.
[36] J. Kriegseis, B. Simon, S. Grundmann, Towards in-flight applications? A review on dielectric barrier discharge-based boundary-layer control, Appl. Mech. Rev. 68 (2) (2016) 020802.
[37] Y.S. Kachanov, V.Y. Levchenko, The resonant interaction of disturbances at laminar-turbulent transition in a boundary layer, J. Fluid Mech. 138 (1984) 209–247.
[38] J. Anemüller, T.J. Sejnowski, S. Makeig, Complex independent component analysis of frequency-domain electroencephalographic data, Neural Netw. 16 (9) (2003) 1311–1323.
[39] J. Anemüller, J.-R. Duann, T.J. Sejnowski, S. Makeig, Spatio-temporal dynamics in fMRI recordings revealed with complex independent component analysis, Neurocomputing 69 (13–15) (2006) 1502–1512.
[40] A. Hyvärinen, P. Ramkumar, L. Parkkonen, R. Hari, Independent component analysis of short-time Fourier transforms for spontaneous EEG/MEG analysis, NeuroImage 49 (1) (2010) 257–271.